

Very long-term relaxation of harmonic 1D self-gravitating systems

Kerwann Tep¹, Jean-Baptiste Fouvry², and Christophe Pichon^{2,3*}

¹ Observatoire Astronomique de Strasbourg, CNRS UMR 7550, 11 rue de l'Université, F-67000 Strasbourg, France

² Institut d'Astrophysique de Paris, CNRS and Sorbonne Université, UMR 7095, 98 bis Boulevard Arago, F-75014 Paris, France

³ Kyung Hee University, Dept. of Astronomy & Space Science, Yongin-shi, Gyeonggi-do 17104, Republic of Korea

March 13, 2026

ABSTRACT

One-dimensional self-gravitating systems admit genuine thermodynamical equilibria. For systems with strictly monotonic orbital frequency profile, the Landau and Balescu–Lenard theories predict a relaxation time scaling linearly with the number of particles, N , in agreement with simulations. Yet, these theories become ill-posed for degenerate frequency profiles, as is the case in the harmonic potential, where all particles share the exact same mean orbital frequency. Using an exact collision-driven 1D integrator, we investigate numerically the self-consistent relaxation of 1D harmonic self-gravitating systems. We show that harmonic systems relax on a timescale that grows quadratically with N . We show that systems that are only partially degenerate display the same quadratic scaling for low N , but transition to the linear, non-degenerate behaviour for larger N . The larger the fraction of degenerate orbits, the larger the value of N at which this transition of dynamical regime occurs. Finally, we explore the dynamics of fully non-degenerate systems, albeit with finite radial support: we confirm that their relaxation time scales linearly with N , though with a substantially larger prefactor than in non-compact systems. Astrophysically, this investigation should offer some new clues on the dynamics of density cores, as in the center of dwarf galaxies.

Key words. Diffusion – Gravitation – Galaxies: kinematics and dynamics – Methods: analytical / numerical

1. Introduction

The dynamics of self-gravitating systems can typically be divided into two phases. First, the system undergoes *violent relaxation* (Lynden-Bell 1967), during which its mean potential rapidly evolves toward a more symmetric configuration. We refer to Chavanis (2022); Ewart et al. (2022) for detailed reviews on this process of *collisionless relaxation*. Following this rapid initial phase, the system ends up dynamically frozen onto some quasi-stationary state, which evolves slowly on long timescales. In isolated long-range interacting systems, this latter phase is captured by the inhomogeneous Balescu–Lenard (BL) equation (Heyvaerts 2010; Chavanis 2012a). This kinetic equation describes how Poisson shot noise, originating from the finite number of particles, drives some long-term relaxation through resonant orbital couplings. Recently, this kinetic theory has shown remarkable success in describing the self-consistent relaxation of self-gravitating systems as diverse as 1D self-gravitating systems (Roule et al. 2022), 2D razor-thin galactic discs (Roule et al. 2025), or 3D globular clusters (Fouvry et al. 2021), to name a few. In all these cases, the system's long-term relaxation is found to occur on a timescale of order $O(N t_{\text{dyn}})$, with N the total number of particles, and t_{dyn} the system's typical dynamical time.

However, the derivation of the Landau and BL equations relies on several key assumptions. In particular, it assumes that the system is not dynamically degenerate, i.e. that the mapping from orbits to their orbital frequencies has a non-zero Jacobian everywhere. In the presence of dynamical degeneracy, these quasilinear

kinetic theories no longer apply, and the long-term behaviour of dynamically degenerate systems remains largely unknown.

In this work, we place our focus on such degenerate systems, whose long-term dynamics we explore numerically. To reduce the numerical complexity of this work, we perform two simplifications: (i) we restrict our analysis to one-dimensional (1D) self-gravitating systems (see, e.g., Miller et al. 2023, for a review); (ii) we consider, first, the most extreme case of a fully degenerate system, namely a harmonic system in which all orbits share the exact same frequency.

Astrophysically, the motivations are two-fold. First, 1D self-gravitating systems are enlightening proxy to model the formation of cosmological large-scale structures (see, e.g., Valageas 2006; Schulz et al. 2013), the subtleties of collisionless relaxation (see, e.g., Joyce & Worrakitpoonpon 2011; Teles et al. 2011; Colombi & Touma 2014), as well as of its collisional counterpart (see, e.g., Joyce & Worrakitpoonpon 2010; Roule et al. 2022), the small-scale gravitational turbulence (see, e.g., Nastac et al. 2025; Ginat et al. 2025), but also the vertical diffusion of stars in galactic discs (see, e.g., Bennett & Bovy 2021; Frankel et al. 2023).

Second, moving from 1D to 3D, harmonic cores are also key to understand the problem of *core stalling*, namely the slow infall of globular clusters to the central core of dwarf galaxies (see, e.g., Inoue 2009; Petts et al. 2016; Kaur & Sridhar 2018, and references therein). Indeed, because they are dynamically degenerate, harmonic cores exhibit a few striking dynamical properties, such as the failure of the classical formula for dynamical friction (Read et al. 2006), some form of super dynamical friction (Zelnikov & Kuskov 2016), friction stalling (Kaur & Stone 2022), and dynamical buoyancy (Banik & van den Bosch 2022).

* Corresponding author: pichon@iap.fr

This short paper is organized as follows. We describe in Section 2 the dynamics of 1D self-gravitating systems, and briefly discuss the collision-driven N -body integrator. We present in Section 3 our method to measure the relaxation timescales. Then, we apply it to various potentials of interest. Finally, we sum up the results in Section 4 and discuss perspective of future projects. Throughout the main text, technical details are kept to a minimum and deferred to Appendices or to relevant references.

2. 1D self-gravitating systems

We are interested in the long-term dynamics of one-dimensional self-gravitating systems. From a numerical perspective, such systems are particularly appealing, as their dynamics can be integrated exactly (up to round-off errors) using a collision-driven N -body integrator (Noulez et al. 2003). This feature allows us to investigate long-term relaxation with tight control over numerical errors.

2.1. Dynamics

We consider a 1D system of N particles on an infinite line, with a total mass equal to M . Throughout this paper, we assume that the cluster comprises particles of equal mass. On top of their individual kinetic energy, we suppose that these particles are subject to 1D gravity described by Poisson equation, $\psi''(x) = 2G\rho(x)$, with $\psi(x)$ the gravitational potential, $\rho(x)$ the mass density and G the gravitational constant. It follows that the gravitational interaction kernel reads

$$U(x, x') = G|x - x'|. \quad (1)$$

The potential felt by a particle i , at location x_i , is then

$$\psi(x_i) = \sum_{j \neq i} m_j U(x_i, x_j) = G \sum_{j \neq i} m_j |x_i - x_j|, \quad (2)$$

where m_j is the mass of the particle j and x_j its position. We note that $\psi(x_i)$ diverges at infinity, hence forbidding any escapers. From this expression, we can compute the force $f_i = -d\psi(x_i)/dx_i$, imposed on the particle i . It reads

$$f_i = G \sum_{j \neq i} m_j \operatorname{sgn}(x_i - x_j) = G(M[>x_i] - M[<x_i]), \quad (3)$$

with $M[<x]$ (resp. $M[>x]$) the total mass enclosed below (resp. above) x . We consider a quasi-stationary system of characteristic extent L . Following the virial theorem (see, e.g., Campa et al. 2014), its characteristic velocity dispersion is $\sigma = \sqrt{GM/L}$. As such, the dynamical time is given by $t_{\text{dyn}} = L/\sigma$. We let $G = M = L = 1$ from now on.

2.2. Time integration

We note that the force in equation (3) is finite – though discontinuous – when the distance between two particles reaches zero. As such, particle crossing is possible – and recurrent – in 1D systems. In the absence of any particle crossing, the force f_i is constant. These two properties are instrumental to construct an exact (up to round-off errors), collision-based integrator. In practice, we are interested in the (very) long-term relaxation of small- N systems. As such, although the integrator is formally exact, one needs to be careful regarding the accumulation of round-off errors. We follow the same approach as Schulz et al. (2013) and

Potential	Compact?	Degenerate?
PLUMMER	No	No
COMPACT	No	Yes
HARMONIC	Yes	Yes
ANHARMONIC	Yes	Partially

Table 1. Quasi-stationary equilibria considered in the numerical simulations. These potentials may have a compact (vs. infinite) radial support, and exhibit some dynamical degeneracy (i.e. particles having the same mean-field orbital frequencies). The presence of dynamical degeneracy impacts critically the long-term relaxation rate of these systems. We refer to Appendix C for their detailed definitions.

use a *double float* precision. This allows us to have particularly well-conserved global invariants (e.g., relative errors of order 10^{-23} , see Figure A.1). This strengthens our confidence in the upcoming numerical explorations. All these aspects are detailed in Appendix A.

2.3. Quasi-stationary equilibria

Our goal is to explore the long-term relaxation of clusters with various dynamical properties, as detailed in Table 1. First, following Roule et al. (2022), we consider PLUMMER: it is both non-degenerate, i.e. all orbits have initially different orbital frequencies, as well as with infinite radial support, i.e. the averaged density is non-zero over the whole real axis. On the contrary, COMPACT is still non-degenerate, but has a compact radial support. Conversely, HARMONIC is a fully degenerate cluster, i.e. all particles have the exact same initial orbital frequency. Additionally, HARMONIC is also of compact support. This peculiar cluster is the one on which most of the upcoming investigation is focused. Finally, we also consider ANHARMONIC. It is of compact support, but with a level of dynamical degeneracy that can be tuned through the parameter ϵ (with $\epsilon = 0$ corresponding to HARMONIC). We refer to Appendix C for the precise definition of each of these equilibria. In practice, we fix units so that, for all potentials, the total energy is $E_{\text{tot}} = \frac{3}{4}GM^2L$ (Appendix B). As such, on average, all these systems converge towards the same thermodynamical distribution.

3. Long-term relaxation

Armed with the potentials from Table 1, we can now address the main question of this work: what is the impact of dynamical degeneracy and/or compact support on the self-consistent long-term relaxation of self-gravitating systems?

3.1. Balescu–Lenard equation

The long-term evolution of finite- N self-gravitating systems is typically described by the inhomogeneous BL equation (Heyvaerts 2010; Chavanis 2012a). In 1D, it takes the form (see, e.g. Roule et al. 2022, for the full equation)

$$\frac{\partial F(E, t)}{\partial t} \propto \frac{1}{N} \frac{\partial}{\partial E} \left[\sum_{k, k'} k \int dE' |U_{kk'}^d|^2 [\dots] \delta_D(k\Omega[E] - k'\Omega[E']) \times \left(k \frac{\partial}{\partial E} - k' \frac{\partial}{\partial E'} \right) F(E, t) F(E', t) \right], \quad (4)$$

with $F(E, t)$ the distribution function of the system, expressed as a function of the individual energy, E . Equation (4) involves a non-local resonance condition, through the Dirac

delta, $\delta_D(k\Omega[E] - k'\Omega[E'])$, with $\Omega(E)$ the orbital frequency. Pairs of particles can interact through the resonance (k, k'), with an efficiency given by the dressed coupling coefficients, $U_{kk'}^d = U_{kk'}^d(E, E', \omega = k\Omega[E])$. Importantly, equation (4) scales like $1/N$. As such, it describes a relaxation occurring on a timescale of order $N t_{\text{dyn}}$.

For HARMONIC, $\Omega(E)$ does not depend on E . As a result, for any resonance $k=k'$, this makes the Dirac delta in equation (4) completely ill-defined. Phrased differently, BL does not apply to HARMONIC, hence leaving the scaling with N of the relaxation time of HARMONIC essentially unconstrained. This is the main motivation for this work: our goal is to explore numerically the self-consistent relaxation of fully degenerate systems, for which the usual (quasilinear) BL kinetic theory does not apply.

3.2. Measuring relaxation

One-dimensional self-gravitating systems admit a well-defined thermodynamical equilibrium (see, e.g., Rybicki 1971), toward which all individual realisations ultimately converge.¹ Hence, the level of a relaxation of any given 1D system can then be assessed through the *distance* between its instantaneous state and its thermodynamical equilibrium.

More precisely, let us consider one realisation of a cluster with N particles. Provided the cluster is recentered around its barycenter, we can take its total momentum to be zero. We denote its total energy with E_{tot} . While E_{tot} is conserved in time, it will change from one realisation to the other. At any given time t , we can measure the cumulative mass function for that realisation, $M(\leq x, t; E_{\text{tot}}, N)$. Following Appendix D, this can be compared with its associated thermodynamical equilibrium $M_{\text{th}}(\leq x; E_{\text{tot}}, N)$, via

$$\delta M(\leq x, t; E_{\text{tot}}, N) = M(\leq x, t; E_{\text{tot}}, N) - M_{\text{th}}(\leq x; E_{\text{tot}}, N). \quad (5)$$

In practice, δM is subject to Poisson fluctuations of order $1/\sqrt{N}$. Ensemble-averaging over N_r realizations yields the average difference

$$\langle \delta M \rangle(\leq x, t) = \langle M(\leq x, t; E_{\text{tot}}, N) - M_{\text{th}}(\leq x; E_{\text{tot}}, N) \rangle. \quad (6)$$

By construction, $\langle \delta M \rangle$ is now subject to (much) smaller statistical fluctuations of order $1/\sqrt{N_r \times N}$ (see Figure A.2). Finally, we compute the Kolmogorov–Smirnov (KS) distance (Conover 1999),

$$D_{\text{KS}}(t) = \sup_{x \in \mathbb{R}} |\langle \delta M \rangle(\leq x, t)|. \quad (7)$$

and define implicitly the effective relaxation time, t_{rel} , via

$$D_{\text{KS}}(t_{\text{rel}}) = D_0, \quad (8)$$

where D_0 is an ad hoc threshold chosen, with care, to yield a statistically significant estimate of t_{rel} . It needs to be smaller than the initial value $D_{\text{KS}}(t=0)$, and larger than the noise floor. For our simulations, numerical testing shows that $D_0=0.015$ and $N_r \times N \sim 10^5$ offer good compromises. In Appendix F, we check that using the larger $D_0=0.022$ does not affect our results.

In Figure 1, we illustrate $D_{\text{KS}}(t)$, as a function of time. In that figure, for the same number of particles N , and the same average

¹ This is in stark contrast with 3D self-gravitating, which, although they continuously relax, do not admit, *stricto sensu*, a thermodynamical equilibrium (see, e.g., Padmanabhan 1990; Chavanis et al. 2002; Katz 2003).

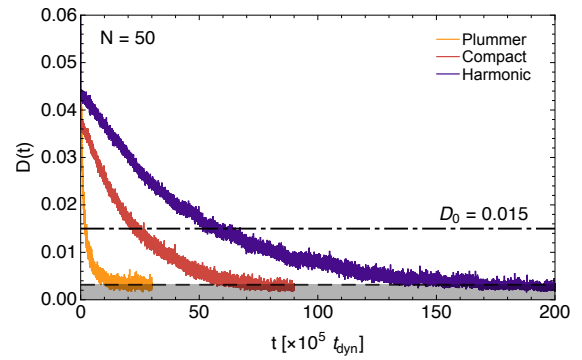


Fig. 1. Time evolution of the KS distance (equation 7) for PLUMMER, COMPACT, and HARMONIC, with $N=50$ and averaged over $N_r=2000$ realizations. The bottom dashed line is the characteristic noise level, $1/\sqrt{N_r \times N}$. The threshold associated with $D_0=0.015$ is given by the dot-dashed line. It is used to estimate the relaxation time, t_{rel} (equation 8). The relaxation times vary greatly between the different potentials, with HARMONIC being the slowest of them all.

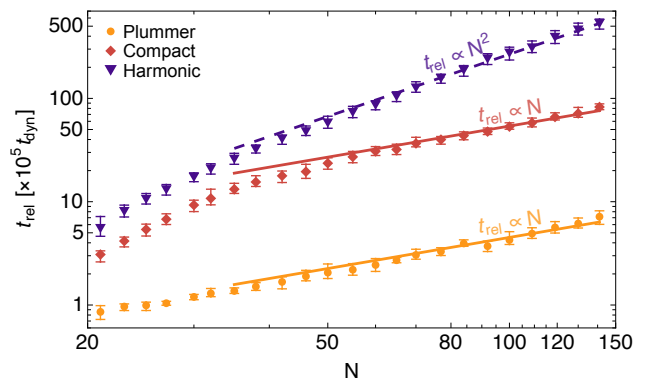


Fig. 2. Dependence of the relaxation time, t_{rel} , with the number of particles, N , for PLUMMER, COMPACT and HARMONIC (Table 1). Both PLUMMER and COMPACT relax on a timescale of order $t_{\text{rel}} \propto N t_{\text{dyn}}$ (solid lines), for N large enough. On the contrary, HARMONIC relaxes on a timescale of order $t_{\text{rel}} \propto N^2 t_{\text{dyn}}$ (dashed line). For small N , measurements are polluted by small- N effects.

total energy $\langle E_{\text{tot}} \rangle$, we observe a significant variation in the relaxation time among the different potentials, with HARMONIC being the slowest. From these time series, and following equation (8), we determine all the crossing times at which the curve $t \rightarrow D_{\text{KS}}(t)$ crosses the threshold D_0 between two sampling points. The relaxation time, t_{rel} , is then estimated as the mean of all crossing times, with the error bar indicating the smallest and largest of these values.

3.3. Application

Let us now investigate numerically the dependence of the relaxation time, t_{rel} , as a function of the considered potentials. In practice, we limited ourselves to the range $21 \leq N \leq 141$, given the prohibitive number of collisions during relaxation, of order $O(N^2 t_{\text{rel}}/t_{\text{dyn}})$, see Appendix A.

First, in Figure 2, we consider PLUMMER, COMPACT and HARMONIC. For N large enough, both PLUMMER and COMPACT exhibit a relaxation time scaling like $t_{\text{rel}} \propto N t_{\text{dyn}}$, with a large prefactor of order 10^5 . This linear dependence in N is fully compatible with BL (equation 4). In addition, for these two systems, $\partial\Omega/\partial E$ is non-zero but small (see Figure C.1). As such, one needs to consider high-order resonances, (k, k'), in equation (4) to comply

with its resonance condition. In parallel, $U_{kk'}^d$ decreases rapidly with (k, k') (see, e.g., figure 6 in Roule et al. 2022). These two properties are responsible for the large prefactor observed in Figure 2, a phenomenon coined *quasi kinetic blocking* in Roule et al. (2022). We also note that COMPACT relaxes about ten times more slowly compared to PLUMMER. This stems from the fact that COMPACT has a narrower range of orbital frequency compared to PLUMMER (see Figure C.1), so that its relaxation is driven by resonances of higher order. PLUMMER and COMPACT differ in their radial support (infinite vs compact), but this does not impact the scaling of the relaxation time. All these features are fully consistent with BL (equation 4).

On the contrary, HARMONIC displays a completely different asymptotic trend in Figure 2. Indeed, HARMONIC relaxes on a timescale scaling like $t_{\text{rel}} \propto N^2 t_{\text{dyn}}$. This is the main result of this paper. Such an (extremely) slow relaxation cannot be explained by BL, since this kinetic equation predicts rather a linear scaling with respect to N .

In 1D systems, relaxation on $N^2 t_{\text{dyn}}$ timescales was already observed in the context of *kinetic blockings* (see, e.g., Fouvy 2022, and references therein). Yet, kinetic blockings fundamentally differ from the relaxation undergone by HARMONIC. Indeed, (i) kinetically blocked systems only sustain $k = k'$ two-body resonances while no such constraint applies to $U_{kk'}^d$, in equation (4). But more importantly, (ii) blocked systems have a strictly monotonic frequency profile, $E \mapsto \Omega(E)$, while HARMONIC has a constant frequency profile. Given these differences, blocked systems have a vanishing BL flux in equation (4), while HARMONIC has a mathematically ill-defined BL flux. Phrased differently, in regard to two-body resonances, blocked systems are *under-resonant*, while HARMONIC is *over-resonant*. In the case of blocked systems, the ultimate relaxation to the thermodynamical equilibrium is driven by three-body resonances. This is captured quantitatively by a $1/N^2$ kinetic equation, see for example equation (4) in Fouvy (2022). Such $1/N^2$ equation is, too, ill-defined for flat frequency profiles, i.e. it does not apply to HARMONIC.

In practice, BL and its $1/N^2$ extensions are all derived from a quasilinear expansion. Crucially, they all rely on a key assumption of phase mixing, which is fundamentally incorrect for HARMONIC. Indeed, within a flat frequency profile, at leading order, particles do not shear away from one another in phase space, making traditional perturbative expansions hopeless. Deriving a closed kinetic equation to describe the self-consistent relaxation of harmonic systems falls beyond the scope of this first numerical exploration. In practice, we expect that the delayed relaxation of HARMONIC is the effective signature of the mechanism of *thermodynamic blocking*, recently put forward in Deme & Fouvy (2025).

In order to strengthen the result from Figure 2, in Figure 3, we consider ANHARMONIC and show the dependence of the relaxation time with N for ANHARMONIC, as one varies ϵ , the fraction of non-degenerate orbits (with $\epsilon=0$ corresponding to HARMONIC). First, we note that as one increases ϵ , relaxation accelerates. In addition, partially degenerate clusters exhibit two scaling regimes for their relaxation time: (i) a scaling like $\propto N^2 t_{\text{dyn}}$ for low N , just like HARMONIC; (ii) a scaling like $\propto N t_{\text{dyn}}$ for large N , just like PLUMMER and COMPACT. This is clear indication that, indeed, dynamical degeneracy delays long-term relaxation. In Figure 3, we note that the value of N at which the transition occurs increases as one decreases ϵ , i.e. as one increases the level of degeneracy of the cluster. Dynamically, this makes sense. Indeed, ANHARMONIC involves initially $N\epsilon$ non-degenerate orbits. At fixed N , increasing ϵ reduces the number of degenerate orbits, hence recovering the usual regime of non-degenerate relax-

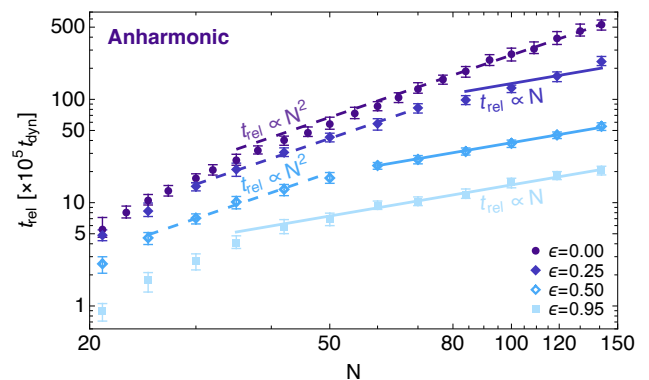


Fig. 3. Same as Figure 2 for ANHARMONIC and various values of ϵ , the level of dynamical degeneracy. As one increases ϵ , the fraction of non-degenerate orbits, the clusters relax faster. Partially degenerate clusters display two relaxation regimes: a relaxation time consistent with $N^2 t_{\text{dyn}}$ (resp. $N t_{\text{dyn}}$) for small (resp. large) N . Increasing ϵ lowers the value of N for which the transition occurs.

ation. Similarly, at fixed ϵ , increasing N increases the number of non-degenerate orbits up to a point where there are enough of them to drive the cluster's overall relaxation. Figures 2 and 3 show jointly how the level of degeneracy directly impacts relaxation timescales. These two figures only offer a first numerical glimpse into the impact of dynamical degeneracy on the long-term relaxation of self-gravitating systems. A thorough theoretical exploration, leveraging in particular techniques from *resonance broadening theory* applied to equation (4) (see, e.g., Dupree 1966; Weinstock 1969; Taylor & McNamara 1971; Dubin 2003), will be the topic of future work.

4. Conclusions and perspectives

4.1. Conclusion

Using an exact collision-driven 1D integrator, we investigated numerically the self-consistent relaxation of one-dimensional harmonic and quasi-harmonic self-gravitating systems. In particular, in Figures 2 and 3, we showed that

- The relaxation time of fully non-degenerate systems, should they be of infinite or compact radial, scales linearly with N . Nonetheless, relaxation occurs with a substantially larger prefactor for compact systems.
- Harmonic systems, because they are dynamically degenerate, exhibit a relaxation time scaling quadratically with N .
- Systems that are partially degenerate display the same quadratic scaling for low N , but transition to a linear, non-degenerate behaviour for larger N .
- The larger the fraction of degenerate orbits, the larger the value of N at which this transition of dynamical regime occurs.

4.2. Perspectives

This work is only a first step toward understanding the relaxation of, possibly dynamically degenerate, long-range interacting systems. We now conclude by mentioning possible venues for future works, focusing first on expected impacts in the astrophysical context.

3D harmonic spheres. As emphasised in Sellwood (2015), the self-consistent relaxation of 3D harmonic globular clusters is greatly delayed compared to their non-degenerate analogues.

Given its prime astrophysical importance, a natural next step is to extend the present investigation to 3D spherical clusters. This could be made using either direct N -body integration codes (see, e.g., Harfst et al. 2007; Wang et al. 2015, 2020), or using approximate methods (see, e.g., Dehnen 2014; Mukherjee et al. 2021; Petersen & Weinberg 2025; Tep et al. 2025) to mitigate the numerical costs.

Dynamical friction. As highlighted in the introduction, harmonic cores are particularly important astrophysically in the context of the *core stalling* problem (see, e.g., Just et al. 2011; Di Cintio & Marcos 2025; Dattathri et al. 2025, and references therein). Here, we focused on self-consistent relaxation. Yet, it would be interesting to investigate whether this delayed harmonic relaxation can provide new insights into the process of dynamical friction, namely the inefficient sinking of globular clusters and satellites in cored halos.

Core dynamics. Putting aside the difference in geometry, we found that harmonic and quasi-harmonic density cores relax much more slowly than standard kinetic theory predicts (see, e.g., Inoue 2009; Petts et al. 2016; Kaur & Sridhar 2018). This affects how long shallow cores in dwarfs can survive and how efficiently they can exchange energy and angular momentum with orbiting substructures. As such, it could prove useful to interpret dynamically off-center active galactic nuclei observed in dwarf galaxies cores, where standard dynamical friction predicts central coalescence.

Inexact integration. All the numerical simulations presented here were performed using an exact integrator (up to round-off errors). Yet, its numerical cost tied us to a rather small range of N in Figures 2 and 3. One should revisit this analysis for larger N , using a faster, but inexact, integration scheme, following Appendix B of Roule et al. (2022). In that case, instantaneous forces are computed exactly in $O(N \ln N)$, through an array sorting. But motion is integrated approximately using a simple leap-frog scheme. Given the large errors made by this integrator (see figure 10 in Roule et al. 2022), performing long-term simulations remains surely challenging numerically.

Multi-mass systems. Here, we restricted our analysis to a single-mass system. Following the approach of Yawn & Miller (1997), it would be interesting to extend this work to multi-mass systems and examine the impact on the self-consistent relaxation of harmonic systems.

Dynamical temperature. Throughout this work, we varied the total number of particles, N , hence varying the amplitude of the Poisson shot-noise fluctuations. Following the approach of Fouvy & Roule (2023), it could be interesting instead to vary the system's dynamical temperature, while keeping N fixed. In practice, this could be achieved by embedding the system within a static background harmonic potential, thereby reducing the level of self-consistency in the fluctuations. Since the dynamics driven by a harmonic potential can be integrated exactly, the present collision-driven integrator could be generalised to this setup while remaining exact, up to round-off errors.

Thermodynamic blocking. Deme & Fouvy (2025) recently emphasised the process of *thermodynamic blocking* in harmonic cores. Namely, when submitted to adiabatic perturbations, i.e. perturbations that maintain the hydrostatic equilibrium, harmonic cores are extremum states of the thermodynamical entropy. At leading order, this prevents heat and matter flows, hence offering some thermodynamical insight on the slow relaxation unveiled in Figure 2. It would be interesting to revisit these results in the context of thermodynamic blocking, possibly predicting a priori the dependence of the relaxation rate with respect to the number of particles.

Time-averaged kinetic theory. In a harmonic core, all orbits share the exact same orbital frequency. As such, one is enticed to describing the system's long-term relaxation by time-averaging the system's Hamiltonian over this one timescale, following an approach similar to Zelnikov & Kuskov (2016). By performing an appropriate canonical transformation, the resulting Hamiltonian closely resembles that of two-dimensional point vortices (see, e.g., Chavanis 2023, and references therein). Such a rewriting could prove useful to understand the delay observed in the self-consistent relaxation of harmonic cores (Figure 2).

Renormalisation theory. On long timescales, after averaging over the orbital period, the dynamics of harmonic cores cannot be described using standard quasilinear techniques, as it no longer sustains phase mixing (see, e.g., Daligault 2011). As such, it is amenable to renormalisation techniques (see, e.g., Krommes 2002, for a thorough review). In that context, the *Direct Interaction Approximation* (see, e.g., Kraichnan 1959; Flores & Fouvy 2025) could offer new clues on self-consistent relaxation.

2D gravity. The dynamics of 2D self-gravitating systems shares deep connexions with the two-dimensional hydrodynamics of point vortices (see, e.g., Chavanis & Lemou 2007; Bouchet & Venaille 2012; Chavanis 2012b, 2023, and references therein). In practice, the associated pairwise interaction diverges on small scales (see, e.g., Fouvy & Chavanis 2025). This could affect the efficiency with which harmonic cores can relax in 2D gravity. This deserves careful numerical exploration, using efficient symplectic integration schemes (see, e.g., Zhang & Qin 1993; San Miguel 2006).

Data availability

The data underlying this article is available through reasonable request to the authors. The code Gravity1D, written in julia (Bezanson et al. 2017) is available at the URL: <https://github.com/KerwannTEP/Gravity1D>.

Acknowledgements

This work is partially supported by the grants ExaSKAle ANR-24-CE31-5182, GALBAR ANR-25-CE31-4684 and BEYOND-BL ANR-25-CE57-2626 of the French Agence Nationale de la Recherche. This project has received financial support from the CNRS through the MITI interdisciplinary programs. This work has made use of the Infinity Cluster hosted by Institut d'Astrophysique de Paris, partially funded by IDF-DIM-ORIGINES-2023-4-11. We thank Stéphane Rouberol for the smooth running of the Infinity cluster.

References

- Banik, U. & van den Bosch, F. C. 2022, *ApJ*, 926, 215
- Bennett, M. & Bovy, J. 2021, *MNRAS*, 503, 376
- Bezanson, J., Edelman, A., Karpinski, S., & Shah, V. B. 2017, *SIAM Review*, 59, 65
- Binney, J. & Tremaine, S. 2008, *Galactic Dynamics: Second Edition* (Princeton Univ. Press)
- Bouchet, F. & Venaille, A. 2012, *Phys. Rep.*, 515, 227
- Campa, A., Dauxois, T., Fanelli, D., & Ruffo, S. 2014, *Physics of long-range interacting systems* (Oxford Univ. Press)
- Chavanis, P.-H. 2012a, *Physica A*, 391, 3680
- Chavanis, P.-H. 2012b, *Physica A*, 391, 3657
- Chavanis, P.-H. 2022, *Physica A*, 606, 128089
- Chavanis, P.-H. 2023, *Europ. Phys. J. Plus*, 138, 136
- Chavanis, P.-H. & Lemou, M. 2007, *Eur. Phys. J. B*, 59, 217
- Chavanis, P.-H., Rosier, C., & Sire, C. 2002, *Phys. Rev. E*, 66, 036105
- Chib, S. & Greenberg, E. 1995, *Am. Stat.*, 49, 327

- Colombi, S. & Touma, J. 2014, MNRAS, 441, 2414
- Conover, W. J. 1999, Practical Nonparametric Statistics, 3rd edn. (New York: John Wiley & Sons)
- Daligault, J. 2011, J. Stat. Phys., 143, 1189
- Dattathri, S., van den Bosch, F. C., Banik, U., et al. 2025, arXiv, 2511.11804
- Dehnen, W. 2014, Comput. Astrophys. Cosmol., 1, 1
- Deme, B. & Fouvry, J.-B. 2025, Universe, 11, 419
- Devroye, L. 1986, Non-Uniform Random Variate Generation (Springer-Verlag)
- Di Cintio, P. & Marcos, B. 2025, A&A, 700, A230
- Dubin, D. H. E. 2003, Phys. Plasmas, 10, 1338
- Dupree, T. H. 1966, Phys. Fluids, 9, 1773
- Ewart, R. J., Brown, A., Adkins, T., & Schekochihin, A. A. 2022, J. Plasma Phys., 88, 925880501
- Flores, S. & Fouvry, J.-B. 2025, Phys. Rev. E, 111, 044111
- Fouvry, J.-B. 2022, Phys. Rev. E, 106, 054123
- Fouvry, J.-B. & Chavanis, P.-H. 2025, Phys. Rev. E, 112, 064113
- Fouvry, J.-B., Hamilton, C., Rozier, S., & Pichon, C. 2021, MNRAS, 508, 2210
- Fouvry, J.-B. & Roule, M. 2023, Phys. Rev. E, 108, 054108
- Frankel, N., Bovy, J., Tremaine, S., & Hogg, D. W. 2023, MNRAS, 521, 5917
- Ginat, Y. B., Nastac, M. L., Ewart, R. J., et al. 2025, Phys. Rev. D, 112, 063501
- Harfst, S., Gualandris, A., Merritt, D., et al. 2007, New. Astron., 12, 357
- Heyvaerts, J. 2010, MNRAS, 407, 355
- Inoue, S. 2009, MNRAS, 397, 709
- Joyce, M. & Worrakitpoonpon, T. 2010, J. Stat. Mech., 2010, 10012
- Joyce, M. & Worrakitpoonpon, T. 2011, Phys. Rev. E, 84, 011139
- Just, A., Khan, F. M., Berczik, P., Ernst, A., & Spurzem, R. 2011, MNRAS, 411, 653
- Katz, J. 2003, Found. Phys., 33, 223
- Kaur, K. & Sridhar, S. 2018, ApJ, 868, 134
- Kaur, K. & Stone, N. C. 2022, MNRAS, 515, 407
- Kraichnan, R. H. 1959, J. Fluid Mech., 5, 497
- Krommes, J. A. 2002, Phys. Rep., 360, 1
- Lynden-Bell, D. 1967, MNRAS, 136, 101
- Miller, B., Manfredi, G., Pirjol, D., & Rouet, J.-L. 2023, Class. Quant. Grav., 40, 073001
- Mukherjee, D., Zhu, Q., Trac, H., & Rodriguez, C. L. 2021, ApJ, 916, 9
- Nastac, M. L., Ewart, R. J., Juno, J., Barnes, M., & Schekochihin, A. A. 2025, arXiv, 2503.17278
- Noullez, A., Fanelli, D., & Aurell, E. 2003, J. Comp. Phys., 186, 697
- Padmanabhan, T. 1990, Phys. Rep., 188, 285
- Petersen, M. & Weinberg, M. 2025, J. Open Source Softw., 10, 7302
- Petts, J. A., Read, J. I., & Gualandris, A. 2016, MNRAS, 463, 858
- Read, J. I., Goerdt, T., Moore, B., et al. 2006, MNRAS, 373, 1451
- Robert, C. & Casella, G. 2004, Monte Carlo Statistical Methods: Second Edition (New York: Springer)
- Roule, M., Fouvry, J.-B., Pichon, C., & Chavanis, P.-H. 2022, Phys. Rev. E, 106, 044118
- Roule, M., Fouvry, J.-B., Pichon, C., & Chavanis, P.-H. 2025, A&A, 699, A140
- Rybicki, G. B. 1971, Ap&SS, 14, 56
- San Miguel, A. 2006, Phys. Rev. E, 74, 046706
- Schulz, A. E., Dehnen, W., Jungman, G., & Tremaine, S. 2013, MNRAS, 431, 49
- Sellwood, J. A. 2015, MNRAS, 453, 2919
- Taylor, J. B. & McNamara, B. 1971, Phys. Fluids, 14, 1492
- Teles, T. N., Levin, Y., & Pakter, R. 2011, MNRAS, 417, L21
- Tep, K., Cook, B. T., Rodriguez, C. L., et al. 2025, ApJ, 993, 180
- Valageas, P. 2006, Phys. Rev. E, 74, 016606
- Wang, L., Iwasawa, M., Nitadori, K., & Makino, J. 2020, MNRAS, 497, 536
- Wang, L., Spurzem, R., Aarseth, S., et al. 2015, MNRAS, 450, 4070
- Weinstock, J. 1969, Phys. Fluids, 12, 1045
- Yawn, K. R. & Miller, B. N. 1997, Phys. Rev. Lett., 79, 3561
- Zelnikov, M. I. & Kuskov, D. S. 2016, MNRAS, 455, 3597
- Zhang, M.-Q. & Qin, M.-Z. 1993, Comput. & Math. Appl., 26, 51

Appendix A: Collision-driven integrator

In this Appendix, we detail our implementation of the exact collision-driven integrator of 1D self-gravitating systems, following the approach from [Noulez et al. \(2003\)](#).

As argued in equation (3), the forces $\{f_i\}_i$ felt by any particles are constant between two collisions. As a result, given the position/velocity of particle i at time t_a , its motion can be integrated exactly. For $t \geq t_a$, as long as it does not undergo any collision, particle i follows the quadratic motion

$$x_i[t] = x_i[t_a] + v_i[t_a](t - t_a) + \frac{1}{2}f_i(t - t_a)^2. \quad (\text{A.1a})$$

$$v_i[t] = v_i[t_a] + f_i(t - t_a), \quad (\text{A.1b})$$

Now, let us assume that particle i collides with some particle $j \geq i$. In 1D self-gravitating systems, particles can cross without issue since the pairwise interaction potential does not diverge for small separation (equation 1). Formally, at the time of collision, we may therefore switch the two particles' indices, velocities and masses, via

$$i \leftrightarrow j \quad ; \quad v_i \leftrightarrow v_j \quad ; \quad m_i \leftrightarrow m_j. \quad (\text{A.2})$$

We also need to compute the updated forces after the collision, following equation (3). Since applying the collision is equivalent to switching indices, the forces are simply updated through the transformation

$$f_i \rightarrow f_i + G(m_i^0 - m_j^0), \quad (\text{A.3a})$$

$$f_j \rightarrow f_j + G(m_i^0 - m_j^0). \quad (\text{A.3b})$$

Meanwhile, particles that are not involved in the collision are left unchanged, and so are the forces they are subject to. From equation (A.3), we point out that the sum of all the forces felt by the system increases by $2(m_i^0 - m_j^0)$ after each crossing of the pair of particles (i, j). In practice, since we only considered systems with equal-mass particles, this did not require any particular numerical care to prevent the growth of numerical errors.

Having dealt with one collision, we now need to determine the time of the subsequent collision, to finalise the algorithm. The naive implementation would be to solve the $(N-1)$ equations on t that read $x_i[t] = x_{i+1}[t]$ for $i=1, \dots, N-1$ (following equation A.1a), and to take the minimum value for t . As pointed out by [Noulez et al. \(2003\)](#), this approach can be drastically accelerated – from a complexity $\mathcal{O}(N)$ to $\mathcal{O}(\ln N)$ – by implementing a heap structure on the particles, ordering them by increasing collision times. We refer to [Noulez et al. \(2003\)](#) for a detailed description of the heap method and its implementation.

Although this integrator is formally exact, it accumulates round-off errors at every collision. These can prove to be a concern for long-term relaxation, hence requiring additional care. Indeed, during one dynamical time, every particle typically crosses every other particle once. Therefore, the system undergoes $\mathcal{O}(N^2)$ collisions per dynamical time (see, e.g., [Joyce & Worrakitpoonpon 2010](#)). As shown in [Roule et al. \(2022\)](#), the typical relaxation time for PLUMMER is of order $t_{\text{rel}} \sim 10^5 t_{\text{dyn}} N$, with the (large) prefactor 10^5 stemming from a *quasi kinetic blocking* inherent to the 1D geometry. As such, to reach thermalisation for PLUMMER, the integrator must go through a (gigantic) number of collisions, of order $\mathcal{O}(10^5 N^3)$. To greatly reduce the impact of round-off error accumulation, we follow [Schulz et al. \(2013\)](#) and use a 80-bit floating-point arithmetic via a double float precision.² This greatly enhances the conservation of the

² In practice, we use the DoubleFloats library from julia (<https://github.com/JuliaMath/DoubleFloats.jl>). It takes advantage of the pre-existing optimizations of double arithmetics.

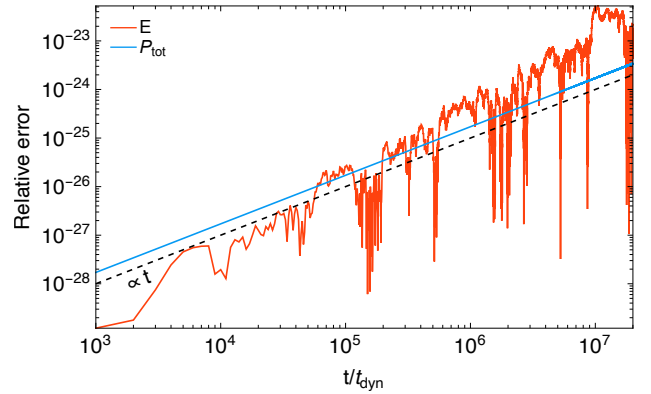


Fig. A.1. Relative error in the total energy (in red) and the total momentum (in blue) during the integration of one HARMONIC cluster with $N=50$, as considered in Figure 1. The errors grow linearly in time (as highlighted by the dashed black line). At $t=2 \times 10^7 t_{\text{dyn}}$, the integrator went through $\sim 6.5 \times 10^9$ collisions for that run.

global invariants (e.g., relative errors of order 10^{-23} instead of 10^{-8}), at the cost of slowing down the code by a factor 4–5.

In Figure A.1, we illustrate the performance of the present scheme, through the conservation of the total energy (equation B.1) and linear momentum ($P_{\text{tot}} = \sum_i m_i v_i$) during the (long-time) integration of HARMONIC. Both invariants exhibit relative errors that are solely driven by round-off errors. Errors increase linearly with time, hinting at some sort of bias in the numerical scheme. Finally, we point out that the use of the 80-bit floating-point arithmetic via a *double float* precision allows us to keep the energy and momentum error below a (very) satisfactory level ($\sim 10^{-23}$) over such long timescales.

In Figure A.2, we illustrate the difference $\langle \delta M \rangle(\leq x, t)$ (equation 6) as a function of time for PLUMMER, COMPACT and HARMONIC. In that figure, we recover their convergence towards the thermodynamical distribution. We note that each potential takes a different time to thermalize, from $t_{\text{rel}} \sim 15 \times 10^5 t_{\text{dyn}}$ for PLUMMER up to $t_{\text{rel}} \sim 200 \times 10^5 t_{\text{dyn}}$ for HARMONIC.

To obtain Figures 2 and 3, we performed simulations using N between 21 and 141. For each value of N , we choose the number of realisations, N_r , so that $N \times N_r \sim 100\,000$. We follow Appendix E to generate the initial conditions. For a given realisation, we dumped the position of the particles every $\Delta t = 1\,000 t_{\text{dyn}}$. In practice, the longest run we performed was for the HARMONIC cluster, with $N=141$. Each integration of this cluster until t_{rel} required ~ 50 h of computation time on a single core. Such a stringent numerical cost is the main reason for our use of a rather limited range of N in Figures 2 and 3.

Appendix B: Integrals of motion

Appendix B.1: Ensemble-averaged total energy

By definition, the exact N -body total energy is the sum of the kinetic energy K and the potential energy V . It reads

$$\begin{aligned} E_{\text{tot}} &= \sum_{i=1}^N \frac{1}{2} m_i v_i^2 + G \sum_{i<j}^N m_i m_j |x_i - x_j| \\ &= K + V. \end{aligned} \quad (\text{B.1})$$

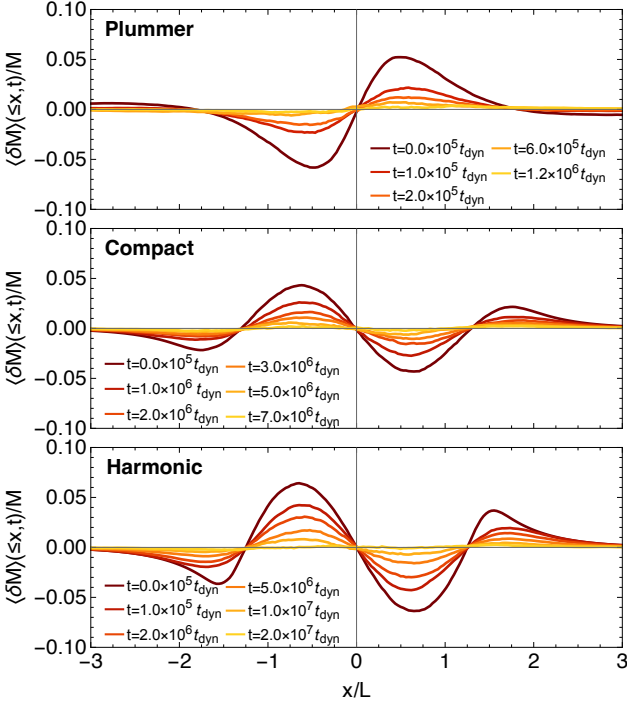


Fig. A.2. Thermalization of the (ensemble-averaged) PLUMMER (top), COMPACT (middle) and HARMONIC (bottom) clusters used to produce Figure 1. Each cluster relaxes towards the $N=50$ thermodynamical distribution, (see Appendix D). The relaxation timescale greatly differs between the considered potentials. For HARMONIC, the sharp edges of the initial density profile are quickly smoothed out.

In the continuum limit, the interaction potential becomes

$$V = \frac{1}{2} \int_{-\infty}^{+\infty} dx \rho(x) \psi(x), \quad (\text{B.2})$$

with $\psi(x)$ and $\rho(x)$, the mean-field potential and density. Applying the virial theorem for 1D self-gravitating clusters (see, e.g., Campa et al. 2014), namely $2K - V = 0$, then yields

$$E_{\text{tot}} = \frac{3}{4} \int_{-\infty}^{+\infty} dx \rho(x) \psi(x). \quad (\text{B.3})$$

Appendix B.2: Orbital frequency

Let us consider a particle with energy E evolving in a fixed symmetric 1D potential, ψ . Its specific energy is

$$E = \frac{1}{2} \dot{x}^2 + \psi(x). \quad (\text{B.4})$$

We can rearrange this equation and obtain

$$\dot{x} = \pm \sqrt{2(E - \psi[x])}. \quad (\text{B.5})$$

It follows that the orbital period of the particle, T , reads

$$\frac{T}{2} = \int_0^{T/2} dt = \int_{-x_a}^{x_a} \frac{dx}{|\dot{x}|} = \int_{-x_a}^{x_a} \frac{dx}{\sqrt{2(E - \psi[x])}}, \quad (\text{B.6})$$

where $x_a > 0$ is the turning radius of the orbit, i.e. it satisfies $\psi(x_a) = E$. Since the orbital frequency Ω satisfies the relation $\Omega T = 2\pi$, we obtain

$$\frac{1}{\Omega} = \frac{1}{\pi} \int_{-x_a}^{x_a} \frac{dx}{\sqrt{2(E - \psi[x])}} = \frac{\sqrt{2}}{\pi} \int_0^{x_a} \frac{dx}{\sqrt{E - \psi(x)}}. \quad (\text{B.7})$$

Appendix C: Quasi-stationary equilibria

In this Appendix, we detail the construction of the various quasi-stationary equilibria considered in the main text. Fortunately, in 1D, this can be made easily using Eddington inversion, as we first recall.

Appendix C.1: Eddington inversion

Applying equation (B.74) of Binney & Tremaine (2008), the DF of a 1D system reads

$$F(E) = -\frac{1}{\pi \sqrt{2}} \int_E^{\infty} \frac{d\Psi}{\sqrt{\Psi - E}} \frac{d\rho}{d\Psi}(x[\Psi]), \quad (\text{C.1})$$

where $x[\Psi]$ is solution of $\Psi = \psi(x)$ and $d\rho/d\Psi = \rho'/\psi'$. Changing the integration variable from Ψ to x yields

$$F(E) = -\frac{1}{\pi \sqrt{2}} \int_{x_a}^{\infty} \frac{dx \rho'(x)}{\sqrt{\psi(x) - E}}, \quad (\text{C.2})$$

where x_a is the boundary of motion, satisfying $E = \psi(x_a)$. We shall also use the notation $F(x_a) = F(x_a[E])$ to refer to this DF.

Using equation (C.2), we are now set to compute the DF of the clusters considered in the main text. In practice, to ease the comparison between the different clusters, following Appendix B.1, for all of them, we set their total energy to $\frac{3}{4} GM^2 L$, with M the cluster's total mass, and L its characteristic length.

Appendix C.2: PLUMMER

We first consider the PLUMMER potential. Following Roule et al. (2022), it reads

$$\rho(x) = \frac{M}{2\alpha} [1 + (x/\alpha)^2]^{-3/2}, \quad (\text{C.3a})$$

$$\psi(x) = E_\alpha \sqrt{1 + (x/\alpha)^2}, \quad (\text{C.3b})$$

$$F(E) = \frac{15M}{32\sqrt{2} \sigma_\alpha \alpha} (E/E_\alpha)^{-7/2}, \quad (\text{C.3c})$$

where $\alpha = 2L/\pi$. We also introduced $\sigma_\alpha = \sqrt{GM\alpha}$, $E_\alpha = GM\alpha$. The total energy is $E_{\text{tot}} = \frac{3\pi}{8} GM^2 \alpha = \frac{3}{4} GM^2 L$. In Figure C.1, we illustrate the associated density.

Appendix C.3: COMPACT

We define the COMPACT density by letting

$$\rho(x) = \frac{M}{Ca} \begin{cases} e^{-a^2/(a^2 - x^2)} & \text{if } |x| < a, \\ 0 & \text{otherwise,} \end{cases} \quad (\text{C.4})$$

with $C = \int_{-1}^1 dy e^{-1/(1-y^2)} \simeq 0.443994$. This corresponds to a compact system, i.e. one with a finite radial support within the domain $|x| \leq a$. Following equation (2), the associated potential reads

$$\psi(x) = GM \begin{cases} \frac{a}{C} \int_{-1}^1 dy |y - x/a| e^{-1/(1-y^2)} & \text{if } |x| < a, \\ |x| & \text{otherwise.} \end{cases} \quad (\text{C.5})$$

Using equation (C.2), we can compute the DF. If $x_a \geq a$, then $F(x_a)$ vanishes. Otherwise, one finds

$$F(x_a) = \frac{M \sqrt{2}}{Ca^2 \pi} \int_{x_a}^a \frac{dx (x/a)}{[1 - (x/a)^2]^2} \frac{e^{-a^2/(a^2 - x^2)}}{\sqrt{\psi(x) - \psi(x_a)}}. \quad (\text{C.6})$$

Finally, we find numerically that the total energy is $E_{\text{tot}} \simeq 0.343104 GM^2 a \simeq \frac{3}{4} GM^2 L$, with $a \simeq 2.18593 L$.

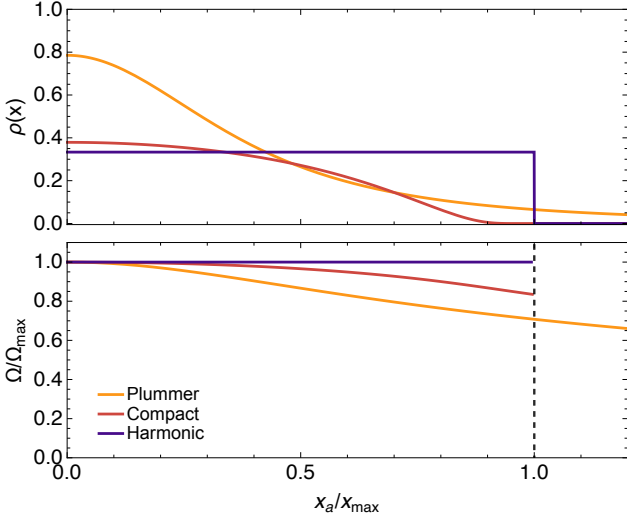


Fig. C.1. Illustration of the density (top panel) and frequency (bottom panel) profiles associated with PLUMMER (Appendix C.2), COMPACT (Appendix C.3) and HARMONIC (Appendix C.4). We define Ω_{\max} as the maximum frequency of each system. We also introduce x_{\max} as the maximum populated pericenter in compact systems, and as $x_{\max} = x_{90\%}$ for PLUMMER, such that $[-x_{90\%}, x_{90\%}]$ contains 90 % of the total mass. The families differ in their finite/infinite radial support, and the presence/absence of dynamical degeneracies.

Appendix C.4: HARMONIC

We now focus on the HARMONIC potential. We consider a system with constant density within the interval $[-a, a]$, where $a = 3L/2$. Using equation (C.2), we have

$$\rho(x) = \frac{1}{2} \frac{M}{a} \Theta(a - |x|), \quad (\text{C.7a})$$

$$\psi(x) = \begin{cases} E_a |x/a| & \text{if } |x| \geq a, \\ \frac{1}{2} E_a + \frac{1}{2} \omega_a^2 x^2 & \text{if } |x| < a, \end{cases} \quad (\text{C.7b})$$

$$F(E) = \frac{M}{2\pi a} \frac{1}{\sqrt{2(GMa - E)}}, \quad (\text{C.7c})$$

where we introduced $E_a = GMa$ and $\omega_a = \sqrt{GM/a}$. The total energy is $E_{\text{tot}} = \frac{1}{2} GM^2 a = \frac{3}{4} GM^2 L$. As expected, HARMONIC has a quadratic potential in its central region. As such, this potential is degenerate: all particles share the same orbital frequency. Indeed, all particles satisfy $x_a \leq a$, so that their individual energy satisfies $E_a/2 \leq E \leq E_a$. Following equation (B.7), we find

$$\frac{1}{\Omega} = \frac{2}{\pi} \sqrt{\frac{a}{GM}} \int_0^{x_a} \frac{dx}{\sqrt{x_a^2 - x^2}} = \sqrt{\frac{a}{GM}}, \quad (\text{C.8})$$

As expected, all particles have the same initial mean-field orbital frequency $\Omega = \omega_a$.

Appendix C.5: ANHARMONIC

We now focus on the ANHARMONIC potentials which are compact but partially degenerate (see Table 1). Given $0 < \epsilon < 1$, we start from the density profile $\rho_\epsilon = \rho_H * \Theta(\epsilon a - |x|)$, where ρ_H is the harmonic density (equation C.7a), $*$ is the convolution operator, and Θ the usual Heaviside function. In practice, one finds that the

density profile reads

$$\rho_\epsilon(x) = \frac{M}{2a} \begin{cases} 1 & \text{if } |x/a| \leq 1 - \epsilon, \\ 0 & \text{if } |x/a| \geq 1 + \epsilon, \\ \frac{1 + \epsilon - |x/a|}{2\epsilon} & \text{otherwise.} \end{cases} \quad (\text{C.9})$$

The associated potential is (equation 2)

$$\psi_\epsilon(x) = GMa \begin{cases} \frac{1}{2} + \frac{\epsilon^2}{6} + \frac{(x/a)^2}{2} & \text{if } |x/a| \leq 1 - \epsilon, \\ |x/a| & \text{if } |x/a| \geq 1 + \epsilon, \\ \frac{1 + 3(\epsilon - |x/a|) + 3(\epsilon + |x/a|)^2 + (\epsilon - |x/a|)^3}{12\epsilon} & \text{otherwise.} \end{cases} \quad (\text{C.10})$$

We can also compute the associated DF. From equation (C.4), we find that the density derivative is

$$\rho'_\epsilon(x) = -\frac{M}{4a^2\epsilon} \begin{cases} \text{sgn}(x/a) & \text{if } 1 - \epsilon \leq |x/a| \leq 1 + \epsilon, \\ 0 & \text{otherwise.} \end{cases} \quad (\text{C.11})$$

We let $\Psi_\pm = \psi_\epsilon[a(1 \pm \epsilon)]$, and introduce $E_{\min} = \psi_\epsilon(0) > 0$. Using equation (C.2), we find

$$F(E) = \frac{M}{4\pi \sqrt{2} a^2 \epsilon} \begin{cases} 0 & \text{if } \Psi_+ < E, \\ \int_{x_a}^{a(1+\epsilon)} \frac{dx}{\sqrt{\psi(x) - E}} & \text{if } \Psi_- \leq E < \Psi_+, \\ \int_{a(1-\epsilon)}^{a(1+\epsilon)} \frac{dx}{\sqrt{\psi(x) - E}} & \text{if } E_{\min} \leq E < \Psi_-. \end{cases} \quad (\text{C.12})$$

In the limit $\epsilon \rightarrow 0^+$, the latter expression becomes a finite difference, to give

$$F(E) = \frac{M}{2\pi \sqrt{2} a} \frac{1}{\sqrt{\psi(a) - E}} = \frac{M}{2\pi a} \frac{1}{\sqrt{2(GMa - E)}}. \quad (\text{C.13})$$

This is exactly the harmonic DF from equation (C.7c). Using equation (B.3), we find that the total energy is

$$E_{\text{tot},\epsilon} = \frac{1}{2} GM^2 a \left(1 + \frac{1}{10} (5 - \epsilon) \epsilon^2\right). \quad (\text{C.14})$$

To ease the comparison between different values of ϵ , we want the total energy not to depend on ϵ . To that end, we consider some (renormalized) pairs of potentials and densities

$$\rho_{\epsilon,A}(x) = A \rho_\epsilon(Ax), \quad (\text{C.15a})$$

$$\psi_{\epsilon,A}(x) = \psi_\epsilon(Ax)/A, \quad (\text{C.15b})$$

whose total mass is M . The associated renormalized DF is simply

$$F_A(x_a) = A^{3/2} F(Ax_a), \quad (\text{C.16})$$

and its total energy is $E_{\text{tot},\epsilon,A} = E_{\text{tot},\epsilon}/A$. Therefore, if we let

$$A = A(\epsilon) = 1 + \frac{1}{10} (5 - \epsilon) \epsilon^2, \quad (\text{C.17})$$

we find $E_{\text{tot},\epsilon,A[\epsilon]} = \frac{1}{2} GM^2 a$. Imposing $a = 3L/2$, we ensure therefore that all ANHARMONIC potentials, independently of their values of ϵ , have the same total energy, $E_{\text{tot}} = \frac{3}{4} GM^2 L$. It is this renormalised family of potentials that is used in the main text. In figure C.2, we illustrate the ANHARMONIC clusters for various values of ϵ .

For a given value of ϵ , the edge of the constant density core is $|x/a| = (1 - \epsilon)/A(\epsilon)$. This edge goes to 1 for $\epsilon \rightarrow 0$, i.e. the fully degenerate harmonic case, and to 0 for $\epsilon \rightarrow 1$, i.e. the fully non-degenerate case. The fraction of particles in the constant density core is $1 - \epsilon$. Therein, the (constant) orbital frequency (equation B.7) is $\Omega = \sqrt{A(\epsilon)} \omega_a$, with ω_a introduced in equation (C.7b).

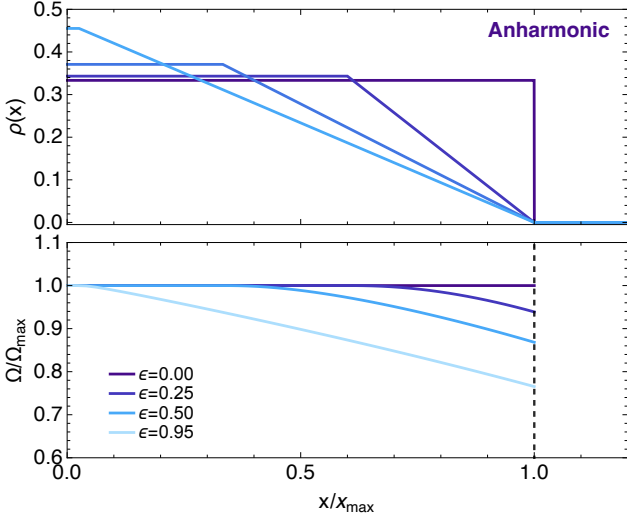


Fig. C.2. Illustration of the ANHARMONIC family for various values of ϵ . We define Ω_{\max} and x_{\max} as in Figure C.1. These systems are of finite radial support, with a central constant density core, i.e. a region that is dynamically degenerate.

Appendix D: Thermodynamical equilibria

In 1D, self-gravitating systems admit genuine thermodynamical equilibria, i.e. the statistical distribution toward which any N -body realisation unavoidably relaxes. It is this distribution that is used in Figure 1 to track long-term relaxation.

Since we are performing simulations with rather small values of N , it is important to obtain the expression of these equilibria while accounting exactly for finite- N effects. Fortunately, this calculation was performed explicitly in Rybicki (1971), whose main results we now reproduce. Let us assume that we are given a realisation of an N -body system with N the total number of particles, E_{tot} the total energy (equation B.1), and a vanishing total linear momentum ($P_{\text{tot}} = \sum_i m_i v_i$).³

Following Rybicki (1971), the exact density profile of the N -particle thermodynamical equilibrium distribution reads

$$\rho_{\text{th}}(x) = \frac{2M}{L} \left(1 - \frac{5}{3N}\right) \sum_{\ell=1}^{N-1} A_{\ell}^{(N)} \left(1 - \frac{4\ell|x/L|}{3N}\right)_+^{\frac{3}{2}N - \frac{7}{2}}, \quad (\text{D.1})$$

where we define $(u)_+ = \max(u, 0)$ and

$$A_{\ell}^{(N)} = \frac{[(N-1)!]^2 (-1)^{\ell-1} \ell}{(N-1-\ell)! (N-1+\ell)!}. \quad (\text{D.2})$$

In the limit $N \rightarrow +\infty$, equation (D.1) becomes the (collisionless) thermodynamical equilibrium distribution (see, e.g., Joyce & Worrakitpoonpon 2010, and references therein)

$$\rho_{\text{th}}(x) = \frac{M}{2} \text{sech}^2(x/L). \quad (\text{D.3})$$

From equation (D.1), we find that the associated cumulative mass distribution, $M_{\text{th}}(x) = \int_{-\infty}^x dy \rho(y)$, reads

$$\begin{aligned} M_{\text{th}}(\leq x) &= \frac{M}{2} \left(1 - \frac{5}{3N}\right) \sum_{\ell=1}^{N-1} \frac{3NA_{\ell}^{(N)}}{\ell} \int_{-\infty}^{4\ell|x/(3LN)} dz (1-|z|)_+^{\frac{3}{2}N - \frac{7}{2}} \\ &= \frac{M}{2} \left(1 - \frac{5}{3N}\right) \sum_{\ell=1}^{N-1} \frac{3NA_{\ell}^{(N)}}{\ell} \mathcal{I}\left[\frac{3}{2}N - \frac{7}{2}, 4\ell|x/(3LN)\right]. \end{aligned} \quad (\text{D.4})$$

³ This can always be assumed through a change of inertial frame.

where, for $\beta > 0$, we introduced

$$\begin{aligned} \mathcal{I}[\beta, w] &= \int_{-\infty}^w dz (1-|z|)_+^{\beta} \\ &= \frac{1}{\beta+1} \begin{cases} (1-|w|)_+^{\beta+1} & \text{if } w < 0, \\ 2 - (1-|w|)_+^{\beta+1} & \text{if } w \geq 0. \end{cases} \end{aligned} \quad (\text{D.5})$$

In practice, the calculation of $A_{\ell}^{(N)}$ in equation (D.1) can be accelerated through the recursion

$$A_1^{(N)} = \frac{N-1}{N}; \quad A_{\ell+1}^{(N)} = \frac{(\ell+1-N)(\ell+1)}{\ell(\ell+N)} A_{\ell}^{(N)}. \quad (\text{D.6})$$

Since $(\ell+1-N)/\ell \leq 1$ and $(\ell+1)/(\ell+N) \leq 1$ for $N \geq 1$, this process is numerically stable.

Appendix E: Generation of initial conditions

In this Appendix, we detail our approach to sample the initial conditions of the N -body realisations. Our goal is to sample N particles $\{(x_i, v_i)\}_i$ for a system with DF $F(E)$, potential $\psi(x)$ and density $\rho(x)$. We can achieve this through two methods. For the sake of completeness, we describe them briefly below.

Appendix E.1: Inverse transform sampling

We consider the spatial cumulative distribution function

$$\text{CDF}_x(x) = \frac{1}{M} \int_{-\infty}^x dx' \rho(x'), \quad (\text{E.1})$$

and the conditional velocity cumulative distribution function

$$\text{CDF}_{v|x}(v|x) = \frac{1}{\rho(x)} \int_{-\infty}^v dv' F(E[x, v']), \quad (\text{E.2})$$

where $E[x, v] = \psi(x) + v^2/2$. We assume that their inverse functions $\text{CDF}_x^{-1}(u_x)$ and $\text{CDF}_{v|x}^{-1}(u_v|x)$ can be computed either analytically or numerically. Then, we can sample each position-velocity pairs via the inverse transform method (Devroye 1986). It proceeds as follows:

1. We draw $u_x \in \mathcal{U}(0, 1)$, from the uniform distribution.
2. We set $x = \text{CDF}_x^{-1}(u_x)$.
3. We draw $u_v \in \mathcal{U}(0, 1)$.
4. We set $v = \text{CDF}_{v|x}^{-1}(u_v|x)$.

In practice, we use this approach for PLUMMER and HARMONIC. Indeed, for PLUMMER, we find from equation (C.3) that

$$\text{CDF}_x(x) = \frac{1}{2} \left(1 + \frac{x}{\sqrt{x^2 + \alpha^2}}\right), \quad (\text{E.3a})$$

$$\text{CDF}_{v|x}(v|x) = \frac{15G^3 M^4 \alpha^2}{32\rho(x)\psi(x)^3} \frac{15s + 20s^3 + 8s^5 + 8(1+s^2)^{5/2}}{15(1+s^2)^{5/2}}, \quad (\text{E.3b})$$

where $s = v/\sqrt{2\psi(x)}$. The inverse for the spatial CDF reads

$$\text{CDF}_x^{-1}(u_x) = \frac{\alpha(2u_x - 1)}{\sqrt{1 - (2u_x - 1)^2}}, \quad (\text{E.4})$$

whereas the inverse for the velocity CDF can be computed numerically using bisection.

For HARMONIC, the spatial sampling reduces to sampling x uniformly over $[-a, a]$. Then, the velocity CDF is given by

$$\text{CDF}_{v|x}(v|x) = \frac{1}{2} + \frac{\arcsin(v/v_{\max}[x])}{\pi}, \quad (\text{E.5})$$

where $v_{\max}^2[x] = E_a - \omega_a^2 x^2$. Its inverse reads

$$\text{CDF}_{v|x}^{-1}(u_v|x) = -v_{\max}[x] \cos(\pi u_v). \quad (\text{E.6})$$

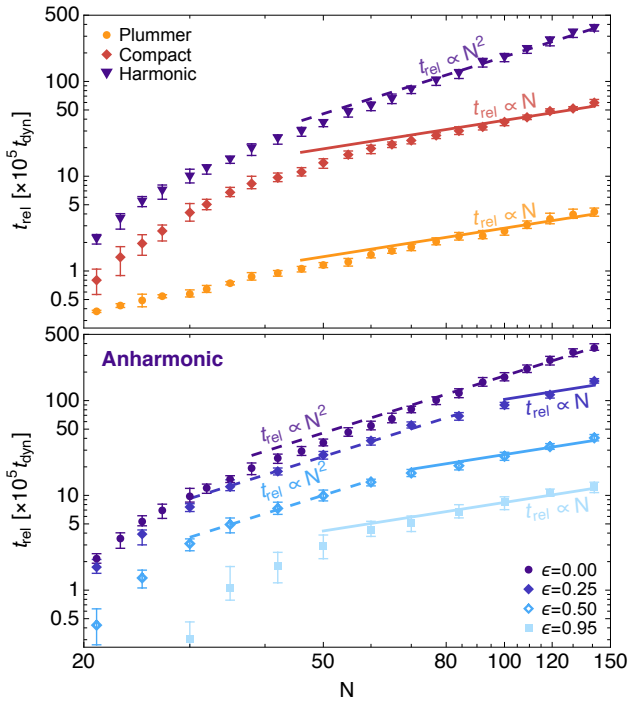


Fig. F.1. Same as Figure 2 (top panel) and Figure 3 (bottom panel), here using the threshold $D_0=0.022$ (equation 8). We recover the exact same trends as in the main text.

Appendix E.2: Rejection sampling

We now suppose that the inverse of the CDF are not available, as is the case for COMPACT and ANHARMONIC. For these systems, we use the von Neumann rejection method (Chib & Greenberg 1995; Robert & Casella 2004). It proceeds as follows.

We wish to sample a random variable \mathcal{R} described by the density $\pi(r)=Kf(r)$, whose normalization constant $K>0$ is unknown. Suppose that \mathcal{R} takes values over a finite interval of size L . We consider the uniform distribution \mathcal{Z} over that interval and the uniform distribution \mathcal{U} over $[0, 1]$. We let \mathcal{M} be an upper bound of $f(r)$ over its interval of definition. Then, we can obtain a sample from $\pi(r)$ through the following algorithm:

1. We generate a proposal, z , from \mathcal{Z} and a value u from \mathcal{U} .
2. If $\mathcal{M}u \leq f(z)$, then we accept the proposal z .
3. If not, we loop back to step 1.

We can now apply this algorithm to generate a pair of position-velocity (x, v) . First, to sample the position, we apply the rejection algorithm to $r \leftarrow x$, $f \leftarrow \rho$ and $\mathcal{M} \leftarrow \max_x \rho(x)$. Then, to sample the velocity, we apply the algorithm to $r \leftarrow v|x$, $f \leftarrow F$ and $\mathcal{M} \leftarrow \max_E F(E)$, where x is the position we just sampled.

Appendix F: Complementary figures

In this Appendix, we complement Figures 2 and 3, by considering a different threshold, D_0 , for the measurements of the relaxation time (as introduced in equation 8). In Figure F.1, we consider the value $D_0=0.022$. As visible in Figure 1, this corresponds to an earlier measurement compared to Figures 2 and 3. Reassuringly, we recover the exact same trends as in the main text, namely (i) the thermodynamic blocking of HARMONIC which relaxes on a timescale of order $\mathcal{O}(N^2)$; (ii) the transition between the two regimes of relaxation for ANHARMONIC, as one varies ϵ , the level of dynamical degeneracy.